ACS APPLIED NANO MATERIALS

www.acsanm.org

Article

Chromium-Doped Nickel Cobaltite Nanoneedles as a Cathodic Material for Li−O_2 Cells: An X-ray Photoemission and Photoabsorption Spectroscopy Investigation

Daniela Giacco, Tomáš Skála, Sergio Brutti, and Andrea G. Marrani*

Cite This: *ACS Appl. Nano Mater.* 2023, 6, 10178−10190

Read Online

ACCESS | Metrics & More | Article Recommendations | Supporting Information

ABSTRACT: Li−O_2 redox chemistry in aprotic electrolytes is promising to boost the performance of secondary batteries, displaying a theoretical energy density more than an order of magnitude higher than the present state-of-the-art Li-ion technology. However, the electrochemical Li_2O_2 formation and dissolution occur in parallel with the so-called ORR and OER (i.e., oxygen reduction reaction and oxygen evolution reaction, respectively), thus requiring suitable electrocatalysts to promote the redox kinetics both in discharge and charge. Here, we discuss the electronic structure and the surface chemistry of a nanoneedle-structured nickel cobaltite doped with chromium as a heterogeneous electrocatalyst for aprotic Li−O_2 cells. A detailed experimental study of the evolution of occupied and unoccupied electronic states of the material from the pristine to a post-mortem condition after operation as a cathode in a Li−O_2 cell is undertaken via ex situ X-ray photoemission (X-ray photoelectron spectroscopy, XPS) and photoabsorption (near-edge X-ray absorption fine structure NEXAFS) spectroscopies. This analysis proved the mixed valence state of the transition metals, their coordination environment within the cobaltite matrix, and their evolution after operation in the cell. In particular, spectroscopic fingerprints of deposition/dissolution phenomena due to solvent degradation were found in the C 1s XP spectra after operation in the Li−O_2 cell, together with an involvement of $Ni^{2+/3+}$ centers in the electrocatalytic processes of oxygen reduction and evolution, enhanced in the presence of a Cr(III) dopant.

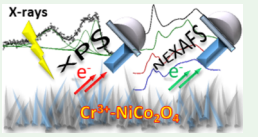

KEYWORDS: *Li−O_2 batteries, X-ray photoemission spectroscopy, X-ray photoabsorption spectroscopy, synchrotron, nickel cobaltite*

1. INTRODUCTION

Aprotic Li−O_2 electrochemical cells have been gaining an increasing interest since the beginning of the XXI century due to their promising theoretical performance (e.g., energy density of 3305 W h kg^{-1}), which outscores by more than one order of magnitude that of more traditional Li-ion batteries.[1,2] The redox reaction exploited in these systems involves the reversible electrochemical formation/dissolution of Li_2O_2 in non-aqueous electrolytes. Unfortunately, the reversibility of these reactions is hindered by various degradation phenomena[3,4] related to the chemical/electrochemical stability of both positive and negative electrodes, electrolytes, and inactive cell constituents upon cycling.[5−7]

The Li_2O_2 electrochemical formation and dissolution take place at the positive electrode, that is usually made of carbon-based materials. In fact, a variety of carbonaceous materials show suitable empty volumes, wettability and porosities to meet all requirements for the build up of a stable triple interface between oxygen gas, liquid electrolyte, and the electrically conductive scaffold, and for the accommodation of the peroxide particles.[8] Besides these multiple functional requirements, carbon-based electrodes catalyze both the oxygen reduction reaction (ORR) and the oxygen evolution reaction (OER).[9,10] On the other hand, carbon-like solid materials can easily promote the formation of CO_2 upon oxidation, thus leading to an irreversible waste of charge and molecular oxygen.

A further step has recently been taken toward non-carbonaceous electrocatalysts for Li−O_2 cells by investigating the use of metal oxides[11,12] with inverse-spinel structures, like nickel cobaltite ($NiCo_2O_4$), which can provide good catalytic activity[13−22] and can be used in C-free self-standing configurations, as we reported recently.[23,24] Remarkably, the use of carbon-free electrocatalysts avoids the degradation of the positive electrode itself upon cycling, that contributes to hamper the overall performance of the device.[6,7] The well-known spinel $NiCo_2O_4$ benefits from the rich redox chemistry of both its nickel and cobalt ions, exhibiting superior electrochemical activity and electrical conductivity, higher than the corresponding parent single-component nickel or cobalt oxides.[25,26] In analogous materials, the superior electrochemical performance has recently been attributed to the presence of oxygen vacancies.[27] Furthermore, $NiCo_2O_4$-based catalysts offer advantages such as natural abundance and low costs compared to noble metals, as well as low toxicity, which make this class of materials suitable candidates for a

Received: March 10, 2023
Accepted: May 30, 2023
Published: June 9, 2023

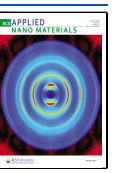

https://doi.org/10.1021/acsanm.3c01087
ACS Appl. Nano Mater. 2023, 6, 10178−10190

Scheme 1. Schematic Representation of the Experimental Procedure for the Synthesis of NCCr Samples

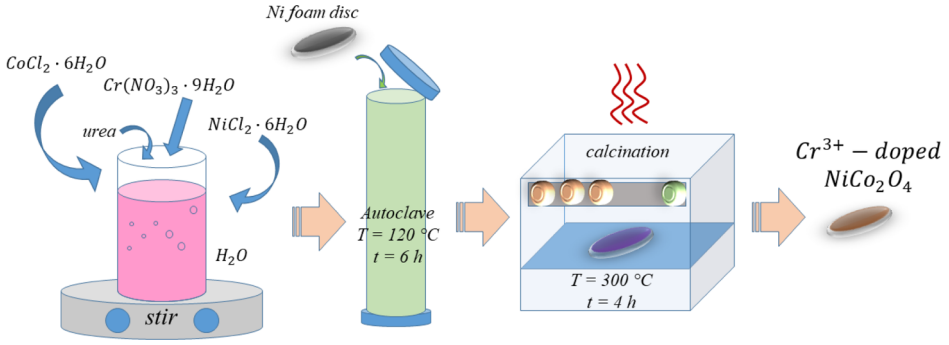

plethora of applications, such as supercapacitors,[25,26,28−33] water splitting,[17−19] and Li-based battery devices.[13−15,34−38]

$NiCo_2O_4$ is a cubic inverse spinel (space group $Fd\bar{3}m$ 227, JCPDS card no. 73-1702) p-type semiconductor with a band gap energy of 2.1 eV,[39] wherein oxygen atoms are distributed in a cubic close-packed lattice, and, according to a generalized view, Ni(II) occupies the octahedral 16d sites and Co(III) is distributed in both the 16d and the tetrahedral 8a sites.[40,41] Even if this picture is generally accepted, the exact distribution of oxidation states among the different metal centers in nickel cobaltite has been debated for long time, with no definitive results reached so far. In fact, upon varying the preparation methods and thermal treatments of the sample, the distribution of +2 and +3 states between Ni and Co and the differently coordinated sites may experience subtle variations. In the seminal work by Goodenough et al.,[42] conducted via neutron diffraction, the structural formula of ferromagnetic $NiCo_2O_4$ was proposed in the form of $Co_{0.35}^{2+}Co_{0.65}^{3+}[Co_1^{3+}Ni_{0.65}^{2+}Ni_{0.35}^{3+}]O_4^{2-}$, where square brackets indicate the octahedral sites and the rest tetrahedral sites. On the other hand, Lenglet's group applied X-ray absorption near-edge spectroscopy (XANES), extended X-ray absorption fine structure (EXAFS), and ^{61}Ni Mössbauer spectroscopy and proposed a more general formula in the form of $Co_x^{2+}Co_{1-x}^{3+}[Co_1^{3+}Ni_{1-x}^{2+}Ni_x^{3+}]O_4^{2-}$, with $x \approx 0.8$.[43] More recent works based on Raman,[44] EXAFS, *K*-edge XANES spectroscopies, and magnetization measurements[45,46] reported other slightly different cation distributions, with Marco et al. proposing an oxidation of Ni close to +4.[46]

Application of X-ray photoelectron spectroscopy (XPS) to routinely assess the chemical composition of $NiCo_2O_4$ has been widely employed, especially in works focused on the application of this material in devices.[13,16,17,19,34,47] Yet, only few attempts have been made in the past to finely interpret the electron ionization features in the Ni 2p and Co 2p regions.[41,46,48−51]

As to the X-ray absorption-related techniques (X-ray absorption spectroscopy, XAS), with a special focus in the vicinity of the ionization threshold, very few reports are present in the literature on $NiCo_2O_4$, mostly investigating the transition metal (TM) *K*-edges.[41,46,52−55] Probing the X-ray absorption at the *L*-edges of TM compounds provides valuable information on the electronic structure of the TM ion in terms of valence and spin state, covalency, ground state symmetry, and ligand properties.

In this work, we discuss for the first time in detail a full X-ray photo-emission/absorption spectroscopic investigation of Cr-(III)-doped $NiCo_2O_4$ needle-like nanostructures, both as pristine material and after operation as electrocatalysts in cathodes for Li−O_2 electrochemical cells. In particular, a detailed analysis of the electronic structure of both nanomaterials has been derived by X-ray-based techniques to shed light on the complex valence and empty states of TMs over the surface of these nanomaterials. The beneficial effect of Cr(III)-doping on the catalytic activity of this material has been recently demonstrated by us by means of galvanostatic cycling in Li−O_2 cells using a LiTFSI/tetraethylene glycol dimethyl ether (TEGDME) electrolyte, and the possible correlation with the electronic structure of the material is here discussed by exploiting ex situ XPS and synchrotron-based near-edge X-ray absorption fine structure (NEXAFS) spectroscopy.

2. EXPERIMENTAL SECTION

2.1. Preparation of Nickel Cobaltite Samples. Cr-doped $NiCo_2O_4$ (NCCr) and undoped $NiCo_2O_4$ (NC) nanoneedles were grown on a nickel mesh starting from $CoCl_2 \cdot 6H_2O$ and $NiCl_2 \cdot 6H_2O$ via an already known hydrothermal method,[36] slightly modified by us to incorporate Cr(III) (see Scheme 1), with details reported elsewhere.[23] The Cr compound used to incorporate Cr atoms in the cobaltite matrix was $Cr(NO_3)_3 \cdot 9H_2O$, with a Cr molar concentration equal to 1/10 of that of Co. Approximately, the cobaltite loading on each disk was ∼1 mg cm^{-2}.[23]

For the spectroscopic experiments, control samples of NiO and Co_3O_4 powder were also used, as commercially purchased from Sigma-Aldrich.

In this study, NCCr samples were characterized both before ("pristine" samples) and after operation in a Li−O_2 cell ("post-mortem" samples).

2.2. Electrochemical Treatment of Nickel Cobaltite Samples. Li−O_2 cell preparation was realized in an Iteco Engineering argon-filled glovebox using ECC-AIR cells by EL-CELL: a metallic lithium coin has been coupled with a glass-fiber separator (Whatman) impregnated with 150 μL cm^{-2} of a non-aqueous electrolyte and the positive electrode. The electrolyte was a 1 molal solution of LiTFSI dissolved in TEGDME (Sigma-Aldrich, moisture-controlled grade). The ∼3 cm^3 dead volume above the positive electrode was filled with +1.1 bar of O_2 (5.0 purity). Electrochemical tests were carried out by using a MTI Corp. battery cycler: currents regimes were set in terms of current densities (*J*) by dividing for the geometrical area of the cathodes (1.54 cm^2).

Galvanostatic cycling of the cells was carried out imposing current density values of 0.1, 0.05, and 0.025 mA cm^{-2} and stopped at cut-off voltages of 2.0 V in discharge and 4.1 V in charge. The measured capacity was normalized dividing by the geometrical area of the cathodes (1.54 cm^2).

After the electrochemical measurements, the cells were disassembled in an Iteco Engineering argon-filled glovebox with a moisture concentration below 0.1 ppm. Their cathodes were recuperated and washed in TEGDME and in tetrahydrofuran (THF) to remove the excess electrolyte, and dried under vacuum at room temperature.

https://doi.org/10.1021/acsanm.3c01087
ACS Appl. Nano Mater. 2023, 6, 10178−10190

2.3. Characterization of Nickel Cobaltite Samples. XP spectra were recorded using a modified Omicron NanoTechnology MXPS system equipped with a monochromatic X-ray source (Omicron XM-1000) and an Omicron EA-125 energy analyzer. The exciting radiation was Al Kα ($h\upsilon$ = 1486.7 eV), generated by operating the anode at 14−15 kV and 10−20 mA. All photoionization regions were acquired using an analyzer pass energy of 20 eV, except for the survey scan, taken at 50 eV pass energy. Take-off angles (θ) of 11° with respect to the sample surface normal were adopted. The measurements were performed at room temperature, and the base pressure in the analyzer chamber was about 2×10^{-9} mbar. The C 1s binding energy (BE) of the $-CH_2-$ groups at 284.8 eV belonging to the aliphatic carbon contamination on the cathode surface was used as an internal standard reference for the BE scale (accuracy of ±0.05 eV). The inelastic mean free path (IMFP) of photoelectrons, λ, was estimated according to the universal curve of inorganic compounds using an average atomic number Z for $NiCo_2O_4$ equal to 16.3.[56] For Ni 2p, Co 2p, and C 1s photoelectrons, the resulting λ was 1.4, 1.5, and 2.3 nm, respectively. As a consequence, the sampling depth $d_{XPS} = 3\lambda \cos\theta$ was 4.1, 4.4, and 6.7 nm, respectively.

Experimental data were fitted using a Shirley function to reproduce the secondary electrons' background and pseudo-Voigt functions for the elastic peaks. These curves are described by a common set of parameters (position, *fwhm*, Gaussian−Lorentzian ratio), which were let free to vary within narrow limits. The Gaussian−Lorentzian ratio was left free to vary between 0.6 and 0.9. Experimentally determined area ratios (with ±10% associated error) were used to estimate XPS atomic ratios between relevant element components, after correction for the corresponding photoionization cross sections according to Scofield calculations[57] and for the square root dependence of the inelastic mean free path from the photoelectron kinetic energy.

NEXAFS spectroscopy experiments at the O *K*-edge and TM *L*-edges were performed at the Materials Science beamline (MSB) of the Elettra synchrotron (Trieste, Italy). MSB, placed at the left end of the bending magnet 6.1, is equipped with *a* plane grating monochromator that provides an estimated 80−90% linearly polarized light in the energy range of 21−1000 eV. The UHV end station, with a base pressure of 2×10^{-10} mbar, is equipped with a Specs Phoibos 150 hemispherical electron analyzer. The electron yield was measured by collecting the primary Auger electrons (Auger electron yield mode, AEY) with kinetic energy in the range (i) 837−852 eV ($L_3M_{45}M_{45}$) for Ni *L*-edge; (ii) 766−780 eV ($L_3M_{45}M_{45}$) for Co *L*-edge; (iii) 523−535 eV ($L_3M_{23}M_{45}$) for Cr *L*-edge; and (iv) 506−519 eV ($KL_{23}L_{23}$) for O *K*-edge. AEY intensity was plotted *vs.* photon energy, and the overall energy resolution was in the range 0.4−0.8 eV for all edges. For the kinetic energies of Auger electrons selected in the given AEY mode experiments λ was estimated to vary within the range 1.25−1.77 nm.[56] The corresponding sampling depth, $d_{NEXAFS} = 3\lambda$, varied in the range 3.75−5.31 nm. Spectra were collected at room temperature and at normal emission with the photon beam incident at 60° off-normal. To eliminate the effect of incident beam intensity fluctuations, the electron yield was normalized using the beam intensity obtained as photocurrent from a gold mesh placed in the beam line. Photon energy scales were calibrated using Au $4f_{7/2}$ and Fermi levels (at BEs 84 and 0 eV, respectively) recorded at different nominal photon energies.

In both XPS and NEXAFS measurements, samples were transferred into the analysis chamber through an argon-filled glove bag connected to the fast-entry lock chamber of the end-station of the beamline in order to avoid contact with air.

Field emission scanning electron microscopy (FE-SEM) experiments were recorded by a Zeiss Auriga electron microscope equipped with a field emission source and a Bruker energy-dispersive X-ray spectroscopy (EDS) probe.

3. RESULTS AND DISCUSSION

3.1. FE-SEM (Pristine Samples). NCCr and NC pristine samples, as grown homogeneously over a nickel mesh, display a morphology based on porous nanoneedles of approximately 50−150 nm in diameter and 1−3 μm in length (Figure 1).[23] These nanoneedles are formed in both cases by highly crystalline polyhedral regular particles with linear size in the 20−30 nm range, as already demonstrated by us in a previous work by X-ray diffraction.[23]

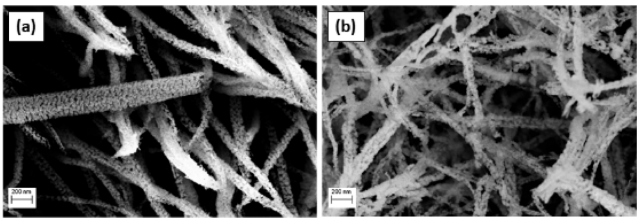

Figure 1. FE-SEM micrographs (100k× magnification) of pristine nanoneedle samples: (a) NC; (b) NCCr. Scale bar is 200 nm.

3.2. XPS (Pristine Samples). Figure 2 reports the Ni $2p_{3/2}$ and Co $2p_{3/2}$ photoionization regions from both NC and NCCr nanoneedle samples. These spectra have been fitted in order to identify the single components related to the several final states which make these profiles so complex. The Ni 2p spectra reveal strict similarities with those of NiO,[58] and the components used to fit the experimental profile are substantially the same as those applicable to that material. The sequence of peaks, together with their BE position and full width at half-maximum (*fwhm*) values, strongly suggest that, similarly to NiO, in NC Ni atoms are predominantly present as Ni^{2+} ions in an O^{2-} O_h ($t_{2g}^6e_g^2$) coordination environment. The fitting parameter set of NiO,[58−61] used to fit the NC and NCCr Ni 2p spectra of Figure 2, implies a six-fold envelope of core-hole final states which are typical of this highly correlated system (see Table S1) and are strongly influenced by charge transfer from the ligand bands to the metal center, including also non-local screening effects between adjacent coordination ensembles.[60,62] The main peak falls around 854.3 eV BE (peak A in Figure 2a,b) and, as in NiO, is related to the most stable charge-transfer final state, termed as $2p^{-1}3d^9L^{-1}$.[59,60] A detailed description of all the peaks in the NiO Ni 2p envelope can be found elsewhere.[58] Even if it generally resembles the complex envelope of NiO final states, the NC Ni 2p spectrum appears also fully compatible with already reported data on $NiCo_2O_4$,[41,46,49,51] this similarity being particularly related to the presence of the second peak around 855.8 eV (red peak B in Figure 2a,b). This feature, according to many authors, could be the fingerprint of Ni(III) centers in spinel phases.[46,51]

Therefore, the Ni 2p XP spectrum of the NC sample shows that Ni^{2+} is not the sole Ni species, but a fraction of low-spin (LS) Ni^{3+} ($t_{2g}^6e_g^1$) centers could be present, this amount being unquantifiable due to overlapping with contributions from Ni^{2+} non-local screening final states at the same BE (red peak B in Figure 2a,b). At the same time, it is evident by comparing the spectra of NC and NCCr samples that Cr-doping results in a reduction of Ni^{3+}concentration at the cobaltite surface. On the other hand, Cr-doping also influences the BE position of both Ni 2p and Co 2p (vide infra) spectral features in the NCCr sample (see Table S1), which appear to be shifted by about 0.35 eV toward higher BE compared to NC. The origin of this behavior is here reported for the first time and can be a clue of a partial polarization of electron density induced by Cr dopant within the metal framework of the spinel matrix.

https://doi.org/10.1021/acsanm.3c01087
ACS Appl. Nano Mater. 2023, 6, 10178−10190

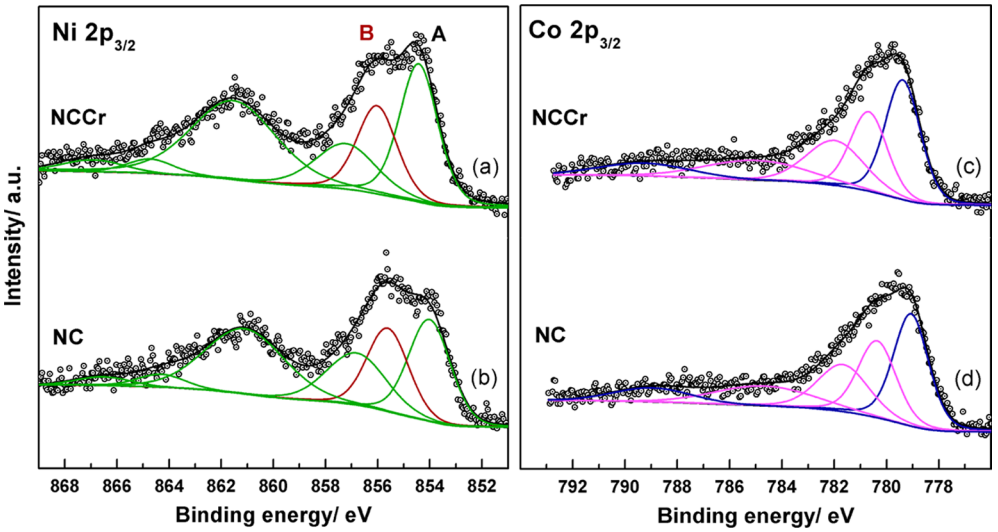

Figure 2. XP spectra in the Ni $2p_{3/2}$ (left) and Co $2p_{3/2}$ (right) regions for NCCr (a,c) and NC (b,d) nanoneedle samples. Experimental data are reported in dots, while peak fitting results are reported in continuous lines. Ni(III) principal component in Ni $2p_{3/2}$ spectra (B) is reported in red (see text), while blue and magenta curves in Co $2p_{3/2}$ are referred to Co(III) and Co(II) components, respectively (see text).

Turning to the Co $2p_{3/2}$ XP region of NC and NCCr nanoneedles, both spectra appear very similar and resemble that of the Co_3O_4 spinel oxide,[63,64] calling for the presence of both Co^{3+} and Co^{2+} sites. In particular, the main peak at 779.3 eV is attributed to a charge-transfer satellite of octahedral LS Co^{3+} ions (t_{2g}^6) in the final state after photoionization ($2p^{-1}3d^7L^{-1}$).[65] The corresponding unscreened final state ($2p^{-1}3d^6$) falls higher in energy, around 789 eV (see blue curves in Figure 2c,d and Table S1).[65−67] The other peaks are all associated to tetrahedral high-spin (HS) Co^{2+} ions ($e^4t_2^3$) in the $2p^{-1}3d^8L^{-1}$, $2p^{-1}3d^9L^{-2}$, and $2p^{-1}3d^7$ final states at increasing binding energy (see magenta curves in Figure 2c,d and Table S1).[65,68] No traces of octahedral HS Co^{2+} ions ($t_{2g}^5e_g^2$) were detected since the intense charge-transfer satellite around 786 eV typical of the CoO phase[65,69] could not be found. Therefore, Co centers in both NC and NCCr samples are constituted by a mixture of octahedral Co^{3+} and tetrahedral Co^{2+} species, with irrelevant differences between the Cr-doped and undoped samples.

XPS also allowed to identify the presence of the chromium dopant, which resulted in a very weak and noisy Cr 2p signal, probably due to a very small concentration of this metal in the spinel matrix. The Cr 2p region, as reported elsewhere,[23] shows the typical 3/2−1/2 spin-orbit split doublet, composed by two broad components centered around 577 and 587 eV, respectively (Figure 3). The position and width of such components suggest that Cr might be present as a mixture of Cr(III) and Cr(IV) species within the spinel matrix.[70−74]

3.3. TM *L*-Edge NEXAFS (Pristine Samples). Whereas XPS was used to probe the occupied states, NEXAFS spectroscopy has been applied to investigate the empty electronic states in the vicinity of the Fermi level (E_F).[75] In this technique, an electron is excited from a core level into a previously unoccupied electronic state above E_F, therefore allowing to obtain a more complete overview on the electronic structure of a compound. Probing the X-ray absorption at the *L*-edges provides valuable information on the electronic structure of the TM ion in terms of valence and spin states, covalency, ground state symmetry, and ligand properties.

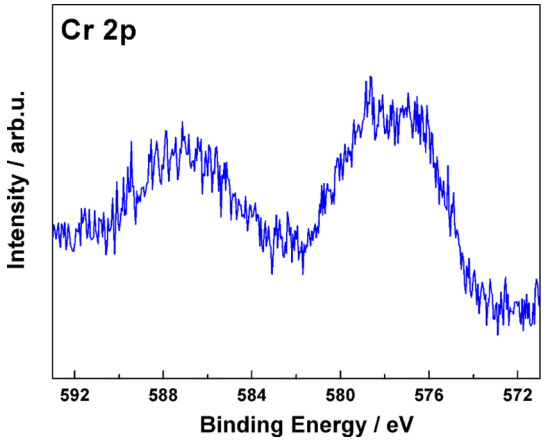

Figure 3. XP spectrum in the Cr 2p region for the NCCr nanoneedle sample.

In Figure 4, the Ni $L_{3,2}$ NEXAFS spectra are shown for the NC and NCCr samples in comparison with the NiO reference. The recorded spectra account for the transitions of the Ni 2p core electron to the corresponding empty 3d orbital. In the case of the Ni $L_{3,2}$-edge, its shape resembles that of NiO

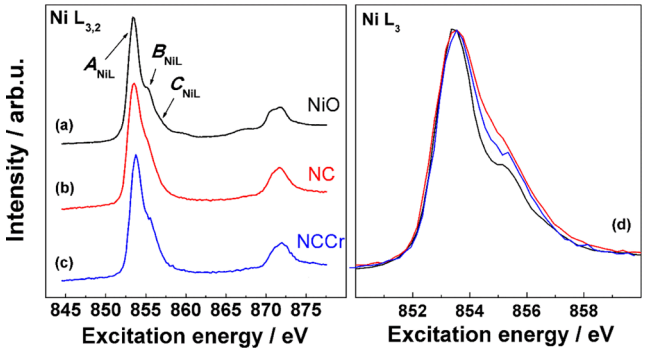

Figure 4. Comparison among Ni $L_{3,2}$ NEXAFS spectra of (a) reference NiO (black), (b) NC (red), and (c) NCCr (blue) samples. (d) Magnified comparison of overlapped spectra in the Ni L_3 region.

https://doi.org/10.1021/acsanm.3c01087
ACS Appl. Nano Mater. 2023, 6, 10178−10190

(Figure 4a) in both NC (Figure 4b) and NCCr (Figure 4c) samples. Therefore, the predominant divalent nature of Ni is confirmed (Ni^{2+}, $t_{2g}^6e_g^2$), with $^3A_{2g}$ symmetry in the ground state.[76] Only the $2p \rightarrow e_g$ transition is dipole allowed, leading to a predominant $2p^5t_{2g}^6e_g^3$ final configuration. The Ni $L_{3,2}$ NEXAFS spectra in Figure 4a–c show a spin–orbit split feature with the L_3 component at ~853 eV and the L_2 one at ~871 eV. The most intense feature (A_{NiL}) in the former component is contributed by multielectron eigenstates related to the $2p_{1/2}^2\ 2p_{3/2}^3\ t_{2g}^6e_g^3$ configuration.[77] The shoulder at ~855 eV (B_{NiL}) arises due to admixture between some of the above mentioned eigenstates with those of the same symmetry related to an electric dipole forbidden two-electron excitation configuration ($2p_{1/2}^2\ 2p_{3/2}^3\ t_{2g}^5e_g^4$).[77,78] In NiO, this admixture allows for the appearance of a further weak bump around 856 eV (C_{NiL}), which partially overlaps with a contribution from a charge transfer final state where the core hole is screened by the ligands ($2p^53d^{10}L^{-1}$).[79]

Comparison among cobaltite samples and reference NiO in the Ni L_3-edge region (Figure 4d) shows that the overall lineshape is very similar, except for a different intensity in the B_{NiL} feature region, which follows this trend: NiO < NCCr < NC. Previously reported theoretical studies showed that Ni sites with an LS Ni^{3+} configuration may contribute intensity in this photon energy region.[76,77,80,81] Therefore, matching the Ni 2p XPS results, the Ni $L_{3,2}$ NEXAFS spectra of NC display a higher content in Ni^{3+} sites compared to NiO, with the NCCr sample being instead more similar to this latter.

Co L-edge NEXAFS spectra of pristine samples and reference Co_3O_4 are reported in Figure 5a–c. The overall

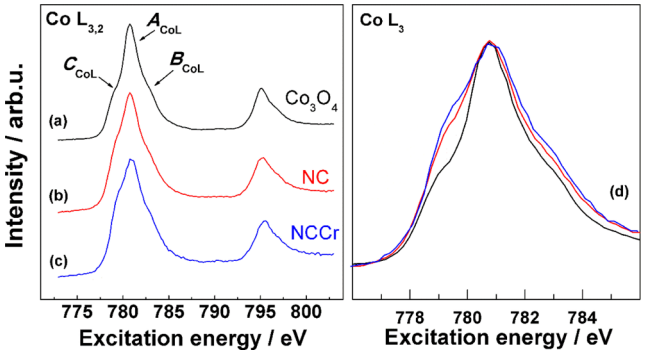

Figure 5. Comparison among Co $L_{3,2}$ NEXAFS spectra of (a) reference Co_3O_4 (black), (b) NC (red), and (c) NCCr (blue) samples. (d) Magnified comparison of overlapped spectra in the Co L_3 region.

lineshape is dominated by the contribution from a LS Co^{3+} (t_{2g}^6, $^1A_{1g}$) species in its ground state configuration, in line with previous observations for mixed spinels used in Li-ion battery applications[82] and theoretically predicted by Montoro et al.[76] For LS Co^{3+} species, the many-electron eigenstates at peak A_{CoL} (at 780.7 eV) are mainly contributed by the final configurations of $2p^5t_{2g}^6e_g^1$, whereas those at peak B_{CoL} (around 783 eV) correspond to $2p^5t_{2g}^5e_g^2$ or higher excitation configurations.[83] A further shoulder can be identified in all samples at the low energy side of the A_{CoL} main peak, here termed C_{CoL} (around 779 eV), typical of the reference spinel Co compound Co_3O_4.[84−86] This feature is mainly contributed by initial state configurations related to HS Co^{2+} in tetrahedral (T_d) coordination ($e^4t_2^3$, $^4A_2$). Upon comparing the three samples in the Co L_3 region (Figure 5d), a modest increase in the C_{CoL} intensity can be observed in the sequence Co_3O_4 < NC < NCCr, calling for an enrichment in Co^{2+} T_d sites in the cobaltite species. It is worth noting that in previously reported Li_xCoO_2 (LCO) materials for Li-ion batteries, the low energy C_{CoL} contribution to the Co L-edge feature has been attributed by various authors to the presence of LS Co^{4+} species (t_{2g}^5), especially under deep Li^+-deintercalation.[76,87,88] Given the different crystal structure of LCO (layered rock salt) vs NC, the presence of Co^{4+} sites can be confidently ruled out in the latter compounds.

In Figure 6 the Cr L-edge NEXAFS spectrum of the NCCr nanoneedles sample is reported, accounting for transitions of

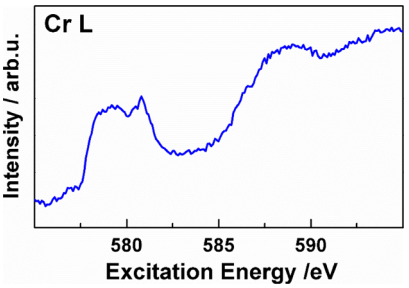

Figure 6. Cr $L_{3,2}$ NEXAFS spectrum of a pristine NCCr nanoneedle sample.

electrons from the Cr 2p to the corresponding empty 3d orbitals. Given the very low concentration of Cr dopant in the spinel structure, the corresponding L-edge spectrum appears very weak in intensity with an unfavorable signal-to-noise ratio. Its profile allows one to discern the two L_3 and L_2 spin–orbit components, the first centered around 580 eV and the second around 590 eV. Both components appear very broad and structured, hinting at a mixture of oxidation states for Cr in the spinel matrix. According to both NEXAFS and XPS spectra of Cr_2O_3 and CrO_2 reported in the literature,[89−93] we suggest that the predominant species is Cr^{3+}, but a fraction of Cr^{4+} may be present as well.

3.4. Oxygen *K*-Edge NEXAFS (Pristine Samples). Given the negligible overlap between the s core-hole and valence wavefunctions, and the small exchange interaction of the 1s core states, X-ray absorption at the O K-edge approximately reflects the partial density of the empty states projected on the adsorbing sites.[75] Figure 7 shows the O K NEXAFS spectra of the nickel cobaltites and reference samples. In general, these spectra can be divided into two main regions, the first ranging between 527 and 534 eV (green-shaded) and the second between 534 and 547 eV. The first generally accounts for electron transitions from the occupied O 1s core states to empty O 2p-Co 3d hybrid states with strong metallic character, while the second implies transitions into O 2p-Co 4s/4p hybrid states, with stronger character of the oxygen ligands. In Co_3O_4, the main peak at 530.8 eV has been mostly attributed to a LS Co^{3+} (t_{2g}^6, $^1A_{1g}$) species in O_h symmetry,[84,94] with no explicit mention to the presence of HS Co^{2+} ions in tetrahedral sites, except in the case of the work by van Elp et al.,[65] where a tentative hypothesis is proposed on the near degeneracy of the four e_g holes of octahedral Co^{3+} and three t_2 holes of tetrahedral Co^{2+} (according to the sequence of spin polarized electronic states for the HS d^7 cation: $(e\uparrow)^2(t_2\uparrow)^3(e\downarrow)^2$). For this reason, the shoulder around 532.5 eV is hypothesized to be due to exchange splitting (as in many TM oxides) occurring

https://doi.org/10.1021/acsanm.3c01087
ACS Appl. Nano Mater. 2023, 6, 10178−10190

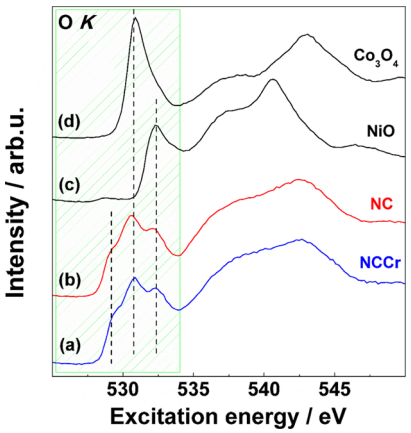

Figure 7. Comparison among O *K* NEXAFS spectra of (a) NCCr (blue), (b) NC (red), and reference (c) NiO and (d) Co_3O_4 (black) samples. Dashed lines in the low-energy region (green shaded) are used as a guide to the eye to better identify the most relevant features.

in the high-spin Co^{2+} species, probably associated to empty minority spin $t_2\downarrow$ states (3 holes available for absorption).[85,94]

In the case of NiO O *K*-edge, one single peak in the "metal" region (green) at 532.3 eV can be identified, corresponding to transitions from O 1s core states to empty O 2p-Ni 3d e_g states of the Ni^{2+} species.[95,96]

As to the two nickel cobaltite samples (NC and NCCr), their O *K* spectra are very similar and display three peaks in the "metal" region. Two of them, at 530.7 and 532.3 eV, are perfectly compatible in position with the main peaks of reference compounds Co_3O_4 and NiO, respectively. This finding confirms the co-presence in nickel cobaltite samples of both Ni^{2+} and Co^{3+}/Co^{2+} sites. The additional peak falls in the low energy region at 529.2 eV for both NC and NCCr compounds. It has seldom been accounted for so far,[52,53] but its intensity appears to depend on the Ni content.[97] Previous studies by Abbate et al. on genuine Ni^{3+} compounds ($LaNiO_3$) have shown that for these materials, a peak is present in the O *K*-edge NEXAFS spectrum, falling at 528.5 eV.[98,99] This feature is considerably lower in energy than that reported for NiO and is attributed to $3d^8L^{-1} \rightarrow c^{-1}3d^8$ transitions (where L^{-1} denotes a hole in the O 2p band screening the initial state, and c^{-1} a O 1s hole after X-ray absorption) related to Ni^{3+} ions in an octahedral oxygen coordination environment. Therefore, in agreement with previous results and the XPS data discussed above, we suggest that the low energy feature in both Cr-doped and undoped nickel cobaltite samples can reasonably be associated to the presence of Ni^{3+} species in an octahedral environment. It is worth mentioning that in the work of Marco et al. on the Ni *K*-edge NEXAFS of $NiCo_2O_4$ obtained by thermal decomposition of metal nitrates, an average Ni-oxidation state of +3.5 was reported, involving the presence of a fraction of Ni^{4+} centers.[46] Nevertheless, in the absence of O *K* NEXAFS measurements on reference genuine Ni^{4+} compounds, we feel more confident in assigning the low energy component to Ni^{3+} in the present case.

Typically, the intensity of the main peak in O *K* NEXAFS spectra is related to bond covalency, since in a purely ionic model where O atoms display a full octet electron configuration, no O 1s → O 2p dipole transition would be allowed. The presence of a covalent bond, allowing for ligand-to-metal charge transfer, renders both these transitions possible and the 3d metal states accessible. The appearance of pre-edge structures may therefore be also related to changes in metal–oxygen bond covalency due to geometry distortion and bond length variations in this type of mixed oxide compared to metal oxide reference compounds.[100] Furthermore, a feature common to both nickel cobaltite samples in contrast to the reference oxide compounds is related to the overall intensity decrease of the peaks in the "metal" region with respect to the high-energy region. In fact, both NC and NCCr display a less intense absorption in the range 527–534 eV, especially compared to the reference Co_3O_4 sample. This result has been attributed to a reduction in the number of metal 3d holes in mixed oxide systems or doped metal monoxides,[94,101] which calls again for a reduced TM 3d-O 2p hybridization.[96] As a consequence, according to the low-energy O *K* spectra, we cannot rule out that our nickel cobaltite samples experience a reduced TM 3d-O 2p covalency compared to the reference NiO and Co_3O_4 samples.

Interestingly, the O *K* NEXAFS spectra of the two nickel cobaltite nanoneedle samples do not display significant differences, despite the results from the Ni *L* and Co *L* NEXAFS spectra. Probably, in our case, the differences between the two samples related to the relative amounts of metal centers in a certain oxidation state and coordination environment result too subtle to be evidenced when the absorption site is not the metal itself.

3.4.1. Post-mortem Studies of NCCr Samples: FE-SEM. NC and NCCr samples have been used as positive electrodes in $Li–O_2$ cells, as reported in the Experimental Section. Ex situ materials have been collected post-mortem from cells tested in galvanostatic cycles at different current densities, i.e., 0.1, 0.05, and 0.025 mA cm^{-2}, and stopped at cut-off voltages of 2.0 V vs Li in discharge, or at 4.1 V vs Li in charge. A detailed discussion on the electrochemical results has been reported previously.[23] Overall, Cr-doping in the $NiCo_2O_4$ spinel strongly boosts the kinetics of the electrochemical ORR and OER in $Li–O_2$ cells: in all electrochemical tests, NCCr electrocatalysts display higher discharge capacity at 2.0 V (~1200 mA h g^{-1} at J = 0.1 mA cm^{-2}) compared to undoped NC (~300 mA h g^{-1} at J = 0.1 mA cm^{-2}), as well as a prolonged cycle life (the areal capacity of 0.2 mA h cm^{-2} is reached at J = 0.1 mA cm^{-2} with a 100% coulombic efficiency for 45 cycles in NCCr, instead of only 1 cycle in NC).[23] On the other hand, the origin of the evident improvement in the electro-kinetics provided by Cr-doping is not understood yet, though, being the morphology of NC and NCCr very similar,[23] an electronic structure-dependent effect is likely to be involved.

In the following, we discuss an ex situ characterization of NCCr samples collected post-mortem from the cells cycled with the three different current densities both after discharge at 2.0 V vs Li and at the end of the first discharge–charge cycle in the range 2.0–4.1 V vs Li. The FE-SEM micrographs recorded on both discharged (left panel) and charged (right panel) NCCr samples are shown in Figure 8.

The morphology of the NCCr electrocatalyst after discharge is strongly altered compared to the pristine state (see Figure 1b compared to 7a–c–e) due to the expected precipitation of Li_2O_2 and the possible accumulation of degradation by-products.[6,7,102] In all cases, the formation of mesoscopic platelet-like morphologies suggests a solvent-mediated crystallization of Li_2O_2 starting from individual nucleation sites with possible lateral merge in larger dendritic structures. The solvent-mediated character of the Li_2O_2 nucleation/growth mechanism is in line with the excellent values of discharge

https://doi.org/10.1021/acsanm.3c01087
ACS Appl. Nano Mater. 2023, 6, 10178–10190

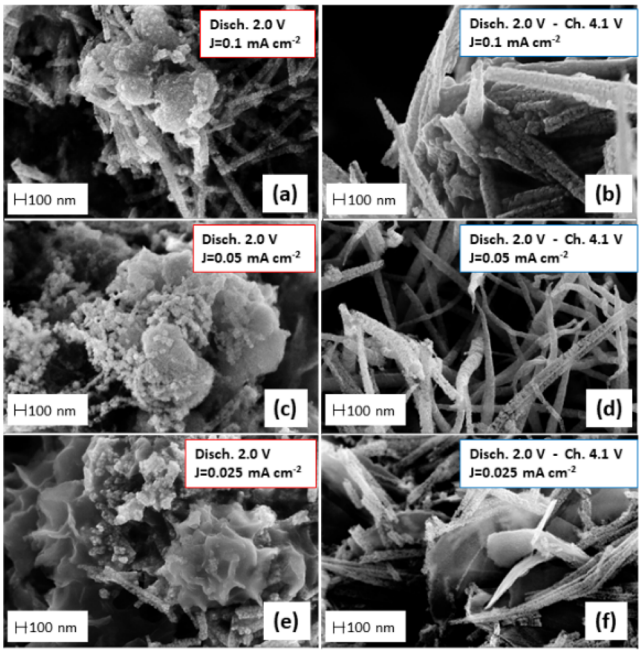

Figure 8. FE-SEM micrographs of discharged (left panel, a,c,e images) and dicharged-charged (right panel, b,d,f images) NCCr electrodes of the LiTFSI/TEGDME Li−O_2 cells addressed in this work. Three different current densities are reported: 0.1 (a,b), 0.05 (c,d), and 0.025 mA cm^{-2} (e,f).

capacities (see ref 23). The morphological homogeneity of the discharge products accumulated over the NCCr electrocatalyst is particularly evident in the samples discharged at 0.025 mA cm^{-2}, where an extended well-formed dendritic-like platelet morphology is observed over the entire surface of the decorated nickel mesh. Besides this dominant morphology, also small prismatic grains are randomly spread over these meso-platelets, possibly due to the de-aggregation upon discharge of the needle-like polycrystalline Cr-doped spinel nickel cobaltite. This morphological degradation of the electrocatalyst is apparently more intense in the case of the NCCr electrode discharged at 0.05 mA cm^{-2}, whereas nanoneedle morphologies are observed almost unaltered in the sample discharged at 0.1 mA cm^{-2}.

Turning to post-mortem morphologies observed after a full discharge/charge cycle, samples collected after cycling at 0.1 and 0.05 mA cm^{-2} show extended needle-like polycrystalline morphologies closely resembling those of the pristine samples. On the other hand, the sample cycled at 0.025 mA cm^{-2} shows the presence of few isolated thin platelet-like morphologies, similar to those observed massively after discharge. This is a possible clue to the irreversible trapping of Li_2O_2 into the electrode, possibly due to poor electronic conduction either originated by pulverization or the accumulation of highly resistive passivation films.

Overall, all post-mortem samples, both after discharge and charge at all current densities, do not show evidence of remarkable electrolyte degradation or accumulation of organic byproducts like in the case of gold-plated nickel mesh[103] or carbonaceous positive electrodes.[7,102] This is a direct evidence of a better selectivity of the NCCr electrocatalyst in the promotion of the ORR and OER reactions with respect to all competitive degradation chemistries. On the other hand, the de-activation of the electrodes after few tens of cycles at all current densities (see ref 23) suggests that degradations occur also on the cobaltite-based electrocatalyst. Being the surface moieties and the nature of the catalytic centers of these

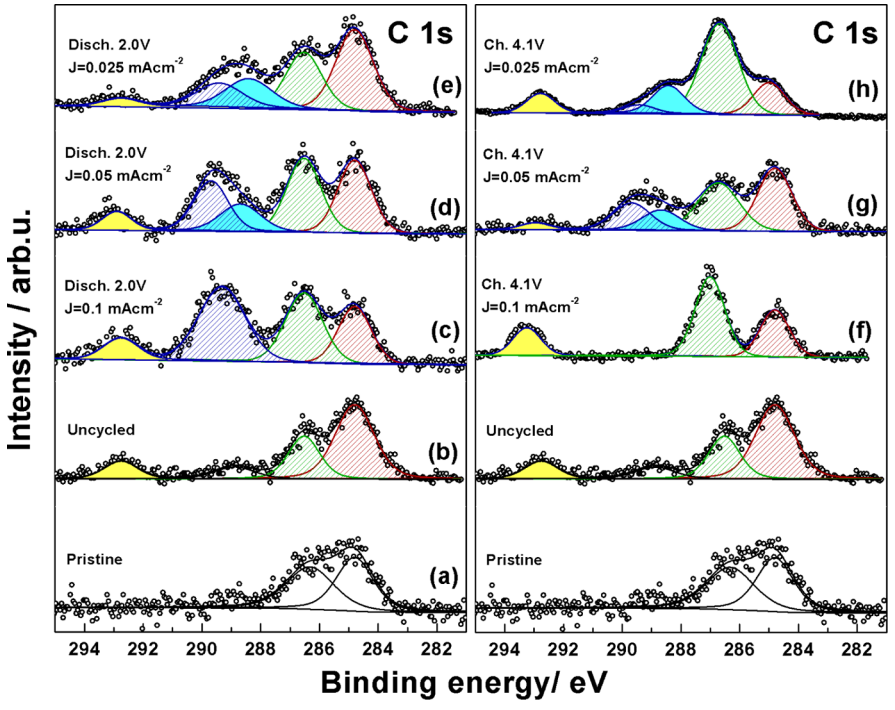

Figure 9. C 1s XP spectra of pristine and uncycled (spectra a,b), discharged (spectra c−e, left panel) and dicharged-charged (spectra f−h, right panel) NCCr electrodes of the LiTFSI/TEGDME Li−O_2 cells addressed in this work. Fitting results are reported as continuous lines. Fitting component color code: red: aliphatic contamination; green: C−O−C in TEGDME; yellow: −CF_3 in LiTFSI; cyan: carboxylate; blue: carbonates. Three different current densities are reported: 0.1 (spectra c,f), 0.05 (spectra d,g), and 0.025 mA cm^{-2} (spectra e,h).

https://doi.org/10.1021/acsanm.3c01087
ACS Appl. Nano Mater. 2023, 6, 10178−10190

electrocatalysts very different, both compared to gold or carbonaceous materials, further spectroscopic analysis is required.

3.5. Post-mortem Studies of NCCr Samples: XPS. In order to shed light on the nature of the surface processes and degradation phenomena taking place over electrodes used in aprotic Li−O_2 cells, the C 1s XP region is particularly valuable.[7,102] In Figure 9 the C 1s photoionization regions are shown before cycling and post-mortem for all tests, both during discharge (left panel) and charge (right panel).

Figure 9a,b (same spectra in both left and right panels) show the C 1s region of reference samples, "pristine" NCCr (dry sample prior to any electrochemical test) and "uncycled" NCCr (sample dried under vacuum after contact with the LiTFSI/TEGDME electrolyte), respectively. The pristine sample shows a weak signal due to the inevitable ambient carbon contamination present in all samples handled in air, composed of a major aliphatic component at 284.8 eV and an oxidized one at 286.3 eV. The first peak is present as well in the "uncycled" sample (Figure 9b, red shaded curve), accompanied by two features attributed to the ethereal carbon atoms in TEGDME solvent (green shaded curve) and −CF_3 groups in LiTFSI salt (yellow filled curve), at 286.5 and 292.8 eV, respectively.[7,102]

The C 1s regions of the discharged NCCr samples are reported in Figure 9c−e at decreasing current density. In all spectra, the features detected in reference samples are always present, though in slightly variable relative amounts. Additionally, in the sample discharged with a 0.1 mA cm^{-2} current density, a new intense feature appears at 289.35 eV (blue shaded curve), attributable to carbonate species.[7,102,104] This same peak appears also in the sample discharged at 0.05 mA cm^{-2} (Figure 9d,e), but is accompanied by the emergence of a lower energy feature at 288.71 eV, which results even more intense in the sample discharged at 0.025 mA cm^{-2}. This feature (cyan-filled curves in Figure 9) can be attributed to carboxylate species.[105] The presence of carbonate and carboxylate species has already been reported by us[6,7,102,103] and other authors in the past,[104,106] and, in both cases, can be associated to degradation phenomena occurring during discharge of the Li−O_2 cell due to chemical or mixed chemical/electrochemical oxidation of carbon-containing species. On the C-free NCCr electrocatalysts, this chemical attack is exerted by the highly reactive oxygen species formed during reduction of molecular O_2 (mainly singlet oxygen, $^1O_2$ and the peroxide species),[3,107] at the expenses of the only carbon-containing compounds, i.e., the TEGDME solvent. Apparently, the increasing intensity of the carboxylate component as the current density decreases suggests a potential-dependent parasitic mechanism; this is a clue of a mixed electrochemical/chemical degradation pathway that leads to carbonates only under high overpotentials. Being singlet oxygen originated in discharge in Li−O_2 cells by the slow LiO_2 disproportion below 2.5 V vs Li,[108] we may speculate that carbonate formation is likely boosted by singlet oxygen formed by superoxide disproportion, whereas carboxylate byproducts possibly form from other reactive channels at higher cathodic overvoltages, e.g., Li_2O_2-mediated solvent degradation.

After a full charge, the surface of the NCCr electrodes is remarkably altered: Figure 9f−h shows the modification of chemical composition within the C 1s region upon oxidation up to 4.1 V vs Li. The use of the highest current density, 0.1 mA cm^{-2}, leads to a full recovery of the initial conditions (see "uncycled" sample), with the apparent complete oxidation of all carbonate deposits accumulated upon discharge: the only reactive channel that can justify this process is the parasitic release of CO_2, a detrimental process that leads to the irreversible consumption of charge and molecular oxygen.[109] Turning to samples charged at lower current densities, both show the presence of residual carbonate/carboxylate species, probably resulting from an incomplete electrochemical oxidation at lower mean overvoltages. This last evidence is in line with the morphological evidence observed by FE-SEM (see Figure 8).

The modifications induced by the electrochemical galvanostatic cycling of NCCr electrocatalysts have been monitored also in the 2p XPS regions of Ni and Co. These spectra show a significantly lower signal-to-noise ratio, especially in the case of discharged samples, which hampers their detection (not shown). This attenuation is most probably related in the discharged samples to the presence of a thick layer of organic material deposited over the NCCr nanoneedle structures, as evidenced both by FE-SEM (Figure 8) and XPS (Figure 9). In accordance with these techniques, the NCCr nanoneedles recovered after charge at 4.1 V did show a Ni 2p and Co 2p detectable, yet lower, intensity, calling for the nearly complete removal of the degradation byproducts accumulated during the discharge phase (Figure S1). The curve-fitting reconstruction of the spectra tested at 0.05 mA cm^{-2} (Figure S1) revealed a modification in the lineshape of the Ni $2p_{3/2}$ spectrum, with an enhancement of the Ni^{3+}-related feature (red-shaded in Figure S1). The reasons behind this phenomenon are unknown, but one may speculate about an active participation of the Ni sites in the OER reaction via Ni^{3+} intermediates, which may remain irreversibly stabilized after cell charge by residual anionic byproducts (carboxylates, carbonates).

3.6. Post-mortem Studies of NCCr Samples: NEXAFS. The post-mortem NEXAFS spectra of NCCr samples discharged at 2.0 V (current density of 0.05 mA cm^{-2}) are reported in Figure S2. In this case, the TM L_3-edge signals are more easily detectable (except Cr L_3, which was too weak) compared to the TM 2p XPS spectra due to the slightly larger sampling depth of NEXAFS vs XPS (see Experimental Section). The Ni and Co L_3 edges in the discharged samples appear with hardly detectable variations with respect to the pristine ones. On the other hand, the O *K*-edge clearly shows a profile compatible with the Li_2CO_3 fingerprint,[110,111] which masks any contribution from the TM-bound O atoms. The presence of such a species is fully compatible with the corresponding C 1s XP spectrum (Figure 9d), showing a prominent carbonate component.

Upon charging the discharged samples up to 4.1 V (Figure 10, current density of 0.025 mA cm^{-2}), all relevant absorption edges, including both Cr L_3 and O *K*, become clear again. These latter edges do not show any significant modifications, except O *K*, which displays a more pronounced feature at 532.5 eV (indicated with a dashed line). As reported above (see Figure 7), this peak can be related to Ni^{2+} centers, probably at the expense of Ni^{3+}. A slight decrease of a Ni^{3+}-related shoulder (B_{NiL}) can be perceived in the Ni L_3-edge (Figure 10, upper left panel) around 855 eV, supporting the increase of Ni^{2+} centers detected in the O *K*-edge. Such a decrease in Ni^{3+} is controversial but may derive from the bulk reduction experienced by the NCCr material during discharge. On the contrary, for the same material, XPS showed an

https://doi.org/10.1021/acsanm.3c01087
ACS Appl. Nano Mater. 2023, 6, 10178−10190

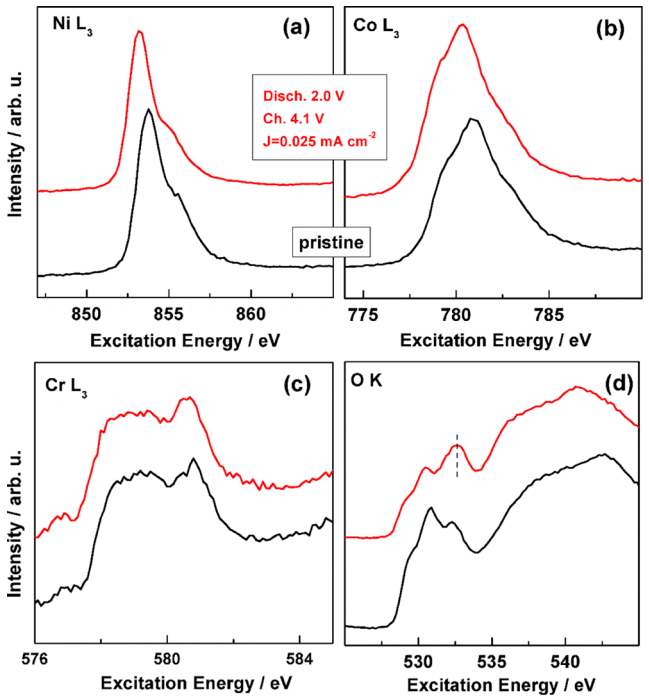

Figure 10. NEXAFS spectra of the discharged-charged (red curves) NCCr electrodes in the (a) Ni L_3, (b) Co L_3, (c) Cr L_3, and (d) O K regions. A comparison with pristine NCCr nanoneedles (black curves) is drawn. The discharge−charge current density is 0.025 mA cm^{-2}.

increase of Ni^{3+} centers (see Figure S1), which are therefore likely confined to the very first surface, after charge.

4. CONCLUSIONS

A detailed X-ray photo-emission/absorption spectroscopic investigation of Cr(III)-doped $NiCo_2O_4$ with needle-like nanostructures has been carried out both on the pristine material and after operation as an electrocatalytic species in cathodes for aprotic Li−O_2 electrochemical cells. XPS allowed one to ascertain the electronic structure and chemical composition of the very first surface layers of the material, with particular regard to the discharged and discharged/charged states of the cathode as a function of current density. The pristine nanoneedles were shown to display a mixture of Ni(II) and Ni(III) LS components in octahedral coordination, with the Cr(III)-doped $NiCo_2O_4$ showing a minor content of Ni(III). Cobalt was found in a mixture of Co(III) (LS, octahedral sites) and Co(II) (HS, tetrahedral sites), with no significant differences between doped and un-doped samples. Synchrotron-based NEXAFS spectra of the TM L-edges substantially confirmed the XPS outcomes, pointing at an enrichment of HS Co(II) in tetrahedral sites for both types of cobaltites compared to the reference Co_3O_4 compound. At the same time, O K-edge NEXAFS spectra revealed a series of contributions which can be traced back to parent reference compounds, such as NiO (Ni^{2+} sites) and Co_3O_4 (Co^{2+}/Co^{3+} sites), with an additional low-energy feature, probably associated to LS Ni(III) sites. A further difference with respect to parent compounds is the lower overall intensity of the cobaltites NEXAFS spectra in the O K region, probably related to a lower TM 3d-O 2p covalency degree in NC and NCCr samples compared to the parent TM oxides.

Upon operation in the electrochemical cell as a cathode, the C 1s XP spectra revealed mixed chemical/electrochemical degradation phenomena of the organic components of the cell (TEGDME solvent) promoted by freshly generated reactive oxygen species during discharge. These byproducts are mixed carboxylate/carbonate species, whose relative amounts are dependent on the current density. A higher current density promotes the formation of carbonate species. Upon charge, the degradation byproducts are oxidized to carbon dioxide with an efficiency directly dependent on the current density. Again, a high current density affords a complete removal of degradation byproducts. The deposition of degradation products after discharge, such as inorganic carbonates, hindered the detection of TM 2p XPS signals, while the O K NEXAFS spectra confirmed the presence of Li_2CO_3. After charge, the Ni $2p_{3/2}$ spectrum showed an enhancement of the Ni^{3+}-related feature at the surface of the electrode, suggesting a possible active participation of the Ni sites in the OER reaction via superficial Ni^{3+} intermediates. As revealed by FE-SEM, NCCr nanoneedle electrodes, both after discharge and charge at all studied current densities, did not show evidence of remarkable electrolyte degradation like in the case of gold-plated nickel mesh or carbonaceous positive electrodes. This points at a higher selectivity of the NCCr electrocatalyst in the promotion of the ORR and OER reactions with respect to all competitive degradation chemistries. According to the above reported spectroscopical evidence, the higher performance of NCCr benefits from the presence of Cr(III) dopant, which apparently decreases the Ni^{3+} concentration in the pristine electrode material, thus fostering the Ni^{2+}/Ni^{3+} redox turnover during the discharge/charge cycles within the Li−O_2 cell.

■ ASSOCIATED CONTENT

Supporting Information

The Supporting Information is available free of charge at https://pubs.acs.org/doi/10.1021/acsanm.3c01087.

Ni 2p and Co 2p XP spectra of discharged/charged samples; NEXAFS spectra of discharged samples; and XPS data (PDF)

■ AUTHOR INFORMATION

Corresponding Author

Andrea G. Marrani − *Dipartimento di Chimica, Università Degli Studi di Roma "La Sapienza", I-00185 Rome, Italy;* orcid.org/0000-0002-3203-9642; Email: andrea.marrani@uniroma1.it

Authors

Daniela Giacco − *Dipartimento di Chimica, Università Degli Studi di Roma "La Sapienza", I-00185 Rome, Italy*

Tomáš Skála − *Faculty of Mathematics and Physics, Charles University, CZ-18000 Prague 8, Czech Republic;* orcid.org/0000-0003-2909-9422

Sergio Brutti − *Dipartimento di Chimica, Università Degli Studi di Roma "La Sapienza", I-00185 Rome, Italy;* orcid.org/0000-0001-8853-9710

Complete contact information is available at: https://pubs.acs.org/10.1021/acsanm.3c01087

Notes

The authors declare no competing financial interest.

https://doi.org/10.1021/acsanm.3c01087
ACS Appl. Nano Mater. 2023, 6, 10178−10190

■ ACKNOWLEDGMENTS

Elettra Synchrotron (Trieste, Italy) is kindly acknowledged for beamtime allocation at the Materials Science Beamline for NEXAFS experiments.

■ REFERENCES

(1) Mahne, N.; Fontaine, O.; Thotiyl, M. O.; Wilkening, M.; Freunberger, S. A. Mechanism and performance of lithium-oxygen batteries-a perspective. *Chem. Sci.* **2017**, *8*, 6716−6729.
(2) Kang, J. H.; Lee, J.; Jung, J. W.; Park, J.; Jang, T.; Kim, H. S.; Nam, J. S.; Lim, H.; Yoon, K. R.; Ryu, W. H.; et al. Lithium-air batteries: Air-breathing challenges and perspective. *ACS Nano* **2020**, *14*, 14549−14578.
(3) Mahne, N.; Schafzahl, B.; Leypold, C.; Leypold, M.; Grumm, S.; Leitgeb, A.; Strohmeier, G. A.; Wilkening, M.; Fontaine, O.; Kramer, D.; et al. Singlet oxygen generation as a major cause for parasitic reactions during cycling of aprotic lithium−oxygen batteries. *Nat. Energy* **2017**, *2*, 17036.
(4) Zou, X.; Lu, Q.; Liao, K.; Shao, Z. Towards practically accessible aprotic Li-air batteries: Progress and challenges related to oxygen-permeable membranes and cathodes. *Energy Storage Mater.* **2022**, *45*, 869−902.
(5) Saito, M.; Fujinami, T.; Yamada, S.; Ishikawa, T.; Otsuka, H.; Ito, K.; Kubo, Y. Effects of Li Salt Anions and O 2 Gas on Li Dissolution/Deposition Behavior at Li Metal Negative Electrode for Non-Aqueous Li-Air Batteries. *J. Electrochem. Soc.* **2017**, *164*, A2872−A2880.
(6) Carboni, M.; Marrani, A. G.; Spezia, R.; Brutti, S. 1,2-Dimethoxyethane Degradation Thermodynamics in Li-O_2 Redox Environments. *Chem.—Eur. J.* **2016**, *22*, 17188−17203.
(7) Giacco, D.; Carboni, M.; Brutti, S.; Marrani, A. G. Noticeable Role of $TFSI^-$ Anion in the Carbon Cathode Degradation of Li-O_2 Cells. *ACS Appl. Mater. Interfaces* **2017**, *9*, 31710−31720.
(8) Liu, L.; Liu, Y.; Wang, C.; Peng, X.; Fang, W.; Hou, Y.; Wang, J.; Ye, J.; Wu, Y. Li_2O_2 Formation Electrochemistry and Its Influence on Oxygen Reduction/Evolution Reaction Kinetics in Aprotic Li−O_2 Batteries. *Small Methods* **2022**, *6*, 2101280.
(9) McCloskey, B. D.; Addison, D. A Viewpoint on Heterogeneous Electrocatalysis and Redox Mediation in Nonaqueous Li-O_2 Batteries. *ACS Catal.* **2017**, *7*, 772−778.
(10) Xia, Q.; Li, D.; Zhao, L.; Wang, J.; Long, Y.; Han, X.; Zhou, Z.; Liu, Y.; Zhang, Y.; Li, Y.; et al. Recent advances in heterostructured cathodic electrocatalysts for non-aqueous Li-O_2 batteries. *Chem. Sci.* **2022**, *13*, 2841−2856.
(11) Zhang, X.; Gong, Y.; Li, S.; Sun, C. Porous Perovskite $La_{0.6}Sr_{0.4}Co_{0.8}Mn_{0.2}O_3$ Nanofibers Loaded with RuO_2 Nanosheets as an Efficient and Durable Bifunctional Catalyst for Rechargeable Li-O_2 Batteries. *ACS Catal.* **2017**, *7*, 7737−7747.
(12) Gong, Y.; Ding, W.; Li, Z.; Su, R.; Zhang, X.; Wang, J.; Zhou, J.; Wang, Z.; Gao, Y.; Li, S.; et al. Inverse Spinel Cobalt-Iron Oxide and N-Doped Graphene Composite as an Efficient and Durable Bifuctional Catalyst for Li-O_2 Batteries. *ACS Catal.* **2018**, *8*, 4082−4090.
(13) Guo, T.; Qin, X.; Hou, L.; Li, J.; Li, X.; Liang, Q. Waxberry-like hierarchical $NiCo_2O_4$ -decorated carbon microspheres as efficient catalyst for Li-O_2 batteries. *J. Solid State Electrochem.* **2019**, *23*, 1359−1369.
(14) Li, L.; Shen, L.; Nie, P.; Pang, G.; Wang, J.; Li, H.; Dong, S.; Zhang, X. Porous $NiCo_2O_4$ nanotubes as a noble-metal-free effective bifunctional catalyst for rechargeable Li-O_2 batteries. *J. Mater. Chem. A* **2015**, *3*, 24309−24314.
(15) Sun, B.; Zhang, J.; Munroe, P.; Ahn, H. J.; Wang, G. Hierarchical $NiCo_2O_4$ nanorods as an efficient cathode catalyst for rechargeable non-aqueous Li-O_2 batteries. *Electrochem. Commun.* **2013**, *31*, 88−91.
(16) Tong, X.; Chen, S.; Guo, C.; Xia, X.; Guo, X. Y. Mesoporous $NiCo_2O_4$ Nanoplates on Three-Dimensional Graphene Foam as an Efficient Electrocatalyst for the Oxygen Reduction Reaction. *ACS Appl. Mater. Interfaces* **2016**, *8*, 28274−28282.
(17) Mahala, C.; Basu, M. Nanosheets of $NiCo_2O_4$/NiO as Efficient and Stable Electrocatalyst for Oxygen Evolution Reaction. *ACS Omega* **2017**, *2*, 7559−7567.
(18) Tao, L.; Li, Y.; Li, M.; Gao, G.; Xiao, X.; Wang, M.; Jiang, X.; Lv, X.; Li, Q.; Zhang, S.; Zhao, Z.; Zhao, C.; Shen, Y. Nanostructured Nickel Cobaltite Antispinel as Bifunctional Electrocatalyst for Overall Water Splitting. *J. Phys. Chem. C* **2017**, *121*, 25888−25897.
(19) Abidat, I.; Morais, C.; Comminges, C.; Canaff, C.; Rousseau, J.; Guignard, N.; Napporn, T. W.; Habrioux, A.; Kokoh, K. B. Three dimensionally ordered mesoporous hydroxylated $Ni_xCo_{3-x}O_4$ spinels for the oxygen evolution reaction: on the hydroxyl-induced surface restructuring effect. *J. Mater. Chem. A* **2017**, *5*, 7173−7183.
(20) Liu, S.; Hu, L.; Xu, X.; Al-Ghamdi, A. A.; Fang, X. Nickel Cobaltite Nanostructures for Photoelectric and Catalytic Applications. *Small* **2015**, *11*, 4267−4283.
(21) Sun, C.; Alonso, J. A.; Bian, J. Recent Advances in Perovskite-Type Oxides for Energy Conversion and Storage Applications. *Adv. Energy Mater.* **2021**, *11*, 2000459.
(22) Bian, J.; Cheng, X.; Meng, X.; Wang, J.; Zhou, J.; Li, S.; Zhang, Y.; Sun, C. Nitrogen-Doped NiCo2O4 Microsphere as an Efficient Catalyst for Flexible Rechargeable Zinc-Air Batteries and Self-Charging Power System. *ACS Appl. Energy Mater.* **2019**, *2*, 2296−2304.
(23) Giacco, D.; Marrani, A. G.; Brutti, S. Enhancement of the performance in Li-O_2 cells of a $NiCo_2O_4$ based porous positive electrode by Cr(III) doping. *Mater. Lett.* **2018**, *224*, 113−117.
(24) Gentile, A.; Giacco, D.; De Bonis, A.; Teghil, R.; Marrani, A. G.; Brutti, S. Synergistic Electro-Catalysis of Pd/PdO Nanoparticles and Cr(III)-Doped $NiCo_2O_4$ Nanofibers in Aprotic Li-O_2 Batteries. *J. Electrochem. Soc.* **2018**, *165*, A3605−A3612.
(25) Zhang, G.; Lou, X. W. General solution growth of mesoporous $NiCo_2O_4$ nanosheets on various conductive substrates as high-performance electrodes for supercapacitors. *Adv. Mater.* **2013**, *25*, 976−979.
(26) Chem, J. M.; Wang, Q.; Liu, B.; Wang, X.; Ran, S.; Wang, L.; Chen, D.; Shen, G. Morphology evolution of urchin-like $NiCo_2O_4$ nanostructures and their applications as pseudocapacitors and photoelectrochemical cells. *J. Mater. Chem.* **2012**, *22*, 21647−21653.
(27) Sadighi, Z.; Huang, J.; Qin, L.; Yao, S.; Cui, J.; Kim, J. K. Positive role of oxygen vacancy in electrochemical performance of $CoMn_2O_4$ cathodes for Li-O_2 batteries. *J. Power Sources* **2017**, *365*, 134−147.
(28) Wang, C.; Zhou, E.; He, W.; Deng, X.; Huang, J.; Ding, M.; Wei, X.; Liu, X.; Xu, X. $NiCo_2O_4$-based supercapacitor nanomaterials. *Nanomaterials* **2017**, *7*, 41.
(29) Li, Y.; Han, X.; Yi, T.; He, Y.; Li, X. Review and prospect of $NiCo_2O_4$-based composite materials for supercapacitor electrodes. *J. Energy Chem.* **2019**, *31*, 54−78.
(30) Cheng, J. P.; Wang, W. D.; Wang, X. C.; Liu, F. Recent research of core−shell structured composites with NiCo2O4 as scaffolds for electrochemical capacitors. *Chem. Eng. J.* **2020**, *393*, 124747.
(31) Yedluri, A. K.; Kim, H. J. Enhanced electrochemical performance of nanoplate nickel cobaltite ($NiCo_2O_4$) supercapacitor applications. *RSC Adv.* **2019**, *9*, 1115−1122.
(32) Lai, H.; Shang, L.; Wu, Q.; Yang, L.; Zhao, J.; Li, H.; Lyu, Z.; Wang, X.; Hu, Z. Spinel Nickel Cobaltite Mesostructures Assembled from Ultrathin Nanosheets for High-Performance Electrochemical Energy Storage. *ACS Appl. Energy Mater.* **2018**, *1*, 684−691.
(33) Dubal, D. P.; Gomez-Romero, P.; Sankapal, B. R.; Holze, R. Nickel cobaltite as an emerging material for supercapacitors: An overview. *Nano Energy* **2015**, *11*, 377−399.
(34) Yuan, J.; Liu, Z.; Wen, Y.; Hu, H.; Zhu, Y.; Thangadurai, V. Hierarchical carbon-free $NiCo_2O_4$ cathode for Li−O_2 batteries. *Ionics* **2019**, *25*, 1669−1677.
(35) Guo, X.; Zhang, J.; Zhao, Y.; Sun, B.; Liu, H.; Wang, G. Ultrathin Porous $NiCo_2O_4$ Nanosheets for Lithium-Oxygen Batteries:

An Excellent Performance Deriving from an Enhanced Solution Mechanism. *ACS Appl. Energy Mater.* **2019**, *2*, 4215−4223.
(36) Lin, X.; Su, J.; Li, L.; Yu, A. Hierarchical porous $NiCo_2O_4$@Ni as carbon-free electrodes for Lithium-oxygen batteries. *Electrochim. Acta* **2015**, *168*, 292−299.
(37) Jadhav, H. S.; Kalubarme, R. S.; Roh, J.-W.; Jung, K.-N.; Shin, K.-H.; Park, C.-N.; Park, C.-J. Facile and Cost Effective Synthesized Mesoporous Spinel $NiCo_2O_4$ as Catalyst for Non-Aqueous Lithium-Oxygen Batteries. *J. Electrochem. Soc.* **2014**, *161*, A2188−A2196.
(38) Han, X.; Gui, X.; Yi, T. F.; Li, Y.; Yue, C. Recent progress of $NiCo_2O_4$-based anodes for high-performance lithium-ion batteries. *Curr. Opin. Solid State Mater. Sci.* **2018**, *22*, 109−126.
(39) Cui, B.; Lin, H.; Liu, Y.; Li, J.; Sun, P.; Zhao, X.; Liu, C. Photophysical and Photocatalytic Properties of Core-Ring Structured $NiCo_2O_4$ Nanoplatelets. *J. Phys. Chem. C* **2009**, *113*, 14083−14087.
(40) Zhao, Q.; Yan, Z.; Chen, C.; Chen, J. Spinels: Controlled Preparation, Oxygen Reduction/Evolution Reaction Application, and Beyond. *Chem. Rev.* **2017**, *117*, 10121−10211.
(41) Marco, J. F.; Gancedo, J. R.; Gracia, M.; Gautier, J. L.; Ríos, E.; Berry, F. J. Characterization of the nickel cobaltite, $NiCo_2O_4$, prepared by several methods: An XRD, XANES, EXAFS, and XPS study. *J. Solid State Chem.* **2000**, *153*, 74−81.
(42) Battle, P. D.; Cheetham, A. K.; Goodenough, J. B. A neutron diffraction study of the ferrimagnetic spinel $NiCo_2O_4$. *Mater. Res. Bull.* **1979**, *14*, 1013−1024.
(43) Lenglet, M.; Guillamet, R.; Dürr, J.; Gryffroy, D.; Vandenberghe, R. E. Electronic structure of $NiCo_2O_4$ by XANES, EXAFS and ^{61}Ni Mössbauer studies. *Solid State Commun.* **1990**, *74*, 1035−1039.
(44) Iliev, M. N.; Silwal, P.; Loukya, B.; Datta, R.; Kim, D. H.; Todorov, N. D.; Pachauri, N.; Gupta, A. Raman studies of cation distribution and thermal stability of epitaxial spinel $NiCo_2O_4$ films. *J. Appl. Phys.* **2013**, *114*, 033514.
(45) Loche, D.; Marras, C.; Carta, D.; Casula, M. F.; Mountjoy, G.; Corrias, A. Cation distribution and vacancies in nickel cobaltite. *Phys. Chem. Chem. Phys.* **2017**, *19*, 16775−16784.
(46) Marco, J. F.; Gancedo, J. R.; Gracia, M.; Gautier, J. L.; Rios, E. I.; Palmer, H. M.; Greaves, C.; Berry, F. J. Cation distribution and magnetic structure of the ferrimagnetic spinel $NiCo_2O_4$. *J. Mater. Chem.* **2001**, *11*, 3087−3093.
(47) Zhang, C.; Deng, L.; Zhang, P.; Ren, X.; Li, Y.; He, T. Mesoporous $NiCo_2O_4$ networks with enhanced performance as counter electrodes for dye-sensitized solar cells. *Dalton Trans.* **2017**, *46*, 4403−4411.
(48) Allen, G. C.; Harris, S. J.; Jutson, J. A.; Dyke, J. M. A study of a number of mixed transition metal oxide spinels using X-ray photoelectron spectroscopy. *Appl. Surf. Sci.* **1989**, *37*, 111−134.
(49) Kim, J.-G.; Pugmire, D. L.; Battaglia, D.; Langell, M. A. Analysis of the $NiCo_2O_4$ spinel surface with Auger and X-ray photoelectron spectroscopy. *Appl. Surf. Sci.* **2000**, *165*, 70−84.
(50) Nydegger, M. W.; Couderc, G.; Langell, M. A. Surface composition of $Co_xNi_{1-x}O$ solid solutions by X-ray photoelectron and Auger spectroscopies. *Appl. Surf. Sci.* **1999**, *147*, 58−66.
(51) Thissen, A.; Ensling, D.; Fernandez Madrigal, F. J.; Jaegermann, W.; Alcantara, R.; Lavela, P.; Tirado, J. L. Photoelectron Spectroscopic Study of the Reaction of Li and Na with $NiCo_2O_4$. *Chem. Mater.* **2005**, *17*, 5202−5208.
(52) Chang, H. W.; Fu, J. X.; Huang, Y. C.; Lu, Y. R.; Kuo, C. H.; Chen, J. L.; Chen, C. L.; Lee, J. F.; Chen, J. M.; Tsai, Y. C.; Ching Chou, W.; Dong, C. L. $NiCo_2O_4$/graphene quantum dots (GQDs) for use in efficient electrochemical energy devices: An electrochemical and X-ray absorption spectroscopic investigation. *Catal. Today* **2020**, *348*, 290−298.
(53) Chang, H. W.; Dong, C. L.; Lu, Y. R.; Huang, Y. C.; Chen, C. L.; Chen, J. L.; Chen, J. M.; Lee, J. F.; Tsai, Y. C. Ex-situ soft X-ray absorption spectroscopic investigation of $NiCo_2O_4$ annealed in different gases for hydrogen generation by electrolysis of urea. *Int. J. Hydrogen Energy* **2019**, *44*, 15771−15778.
(54) Chadwick, A. V.; Savin, S. L. P.; Fiddy, S.; Alcantara, R.; Fernández Lisbona, D.; Lavela, P.; Ortiz, G. F.; Tirado, J. L. Formation and oxidation of nanosized metal particles by electrochemical reaction of Li and Na with $NiCo_2O_4$: X-ray absorption spectroscopic study. *J. Phys. Chem. C* **2007**, *111*, 4636−4642.
(55) Deeloed, W.; Hanlumyuang, Y.; Limphirat, W.; Suramitr, S.; Chansaenpak, K.; Kanjanaboos, P.; Wannapaiboon, S.; Wattanathana, W. Oxidative thermal conversion of hydrothermal derived precursors toward the mixed-metal cobaltite spinel oxides ($ZnCo_2O_4$ and $NiCo_2O_4$): In-situ investigation by synchrotron-radiation XRD and XAS techniques. *Crystals* **2021**, *11*, 1256.
(56) Seah, M. P. An accurate and simple universal curve for the energy-dependent electron inelastic mean free path. *Surf. Interface Anal.* **2012**, *44*, 497−503.
(57) Scofield, J. H. Hartree-Slater subshell photoionization cross-sections at 1254 and 1487 eV. *J. Electron Spectrosc. Relat. Phenom.* **1976**, *8*, 129−137.
(58) Marrani, A. G.; Novelli, V.; Sheehan, S.; Dowling, D. P.; Dini, D. Probing the Redox States at the Surface of Electroactive Nanoporous NiO Thin Films. *ACS Appl. Mater. Interfaces* **2014**, *6*, 143−152.
(59) Van Elp, J.; Eskes, H.; Kuiper, P.; Sawatzky, G. A. Electronic structure of Li-doped NiO. *Phys. Rev. B: Condens. Matter Mater. Phys.* **1992**, *45*, 1612−1622.
(60) Van Veenendaal, M. A.; Sawatzky, G. A. Nonlocal screening effects in 2p x-ray photoemission spectroscopy core-level line shapes of transition metal compounds. *Phys. Rev. Lett.* **1993**, *70*, 2459−2462.
(61) Mossanek, R. J. O.; Preda, I.; Abbate, M.; Rubio-Zuazo, J.; Castro, G. R.; Vollmer, A.; Gutiérrez, A.; Soriano, L. Investigation of surface and non-local screening effects in the Ni 2p core level photoemission spectra of NiO. *Chem. Phys. Lett.* **2011**, *501*, 437−441.
(62) Alders, D.; Voogt, F.; Hibma, T.; Sawatzky, G. A. Nonlocal screening effects in 2p x-ray photoemission spectroscopy of NiO (100). *Phys. Rev. B: Condens. Matter Mater. Phys.* **1996**, *54*, 7716−7719.
(63) Gautier, J. L.; Rios, E.; Gracia, M.; Marco, J. F.; Gancedo, J. R. Characterisation by X-ray photoelectron spectroscopy of thin $Mn_xCo_{3-x}O_4(1\geq x\geq 0)$ spinel films prepared by low-temperature spray pyrolysis. *Thin Solid Films* **1997**, *311*, 51−57.
(64) Chuang, T. J.; Brundle, C. R.; Rice, D. W. Interpretation of the x-ray photoemission spectra of cobalt oxides and cobalt oxide surfaces. *Surf. Sci.* **1976**, *59*, 413−429.
(65) van Elp, J.; Wieland, J. L.; Eskes, H.; Kuiper, P.; Sawatzky, G. A.; de Groot, F. M. F.; Turner, T. S. Electronic structure of CoO, Li-doped CoO, and $LiCoO_2$. *Phys. Rev. B: Condens. Matter Mater. Phys.* **1991**, *44*, 6090−6103.
(66) Kolotyrkin, Y. M.; Belova, I. D.; Roginskaya, Y. E.; Kozhevnikov, V. B.; Zakhar'in, D. S.; Venevtsev, Y. N. High-spin configuration of Co(III) in nonstoichiometric Co_3O_4 films. XPS investigations. *Mater. Chem. Phys.* **1984**, *11*, 29−48.
(67) Galakhov, V. R.; Karelina, V. V.; Kellerman, D. G.; Gorshkov, V. S.; Ovechkina, N. A.; Neumann, M. Electronic structure, x-ray spectra, and magnetic properties of the $LiCoO_{2-\delta}$ and Na_xCoO_2 nonstoichiometric oxides. *Phys. Solid State* **2002**, *44*, 266−273.
(68) Reddy, K. P.; Jain, R.; Ghosalya, M. K.; Gopinath, C. S. Metallic cobalt to spinel Co_3O_4-electronic structure evolution by near-ambient pressure photoelectron spectroscopy. *J. Phys. Chem. C* **2017**, *121*, 21472−21481.
(69) Kim, K. S. X-ray-photoelectron spectroscopic studies of the electronic structure of CoO. *Phys. Rev. B: Solid State* **1975**, *11*, 2177−2185.
(70) Sainio, J.; Aronniemi, M.; Pakarinen, O.; Kauraala, K.; Airaksinen, S.; Krause, O.; Lahtinen, J. An XPS study of CrO_x on a thin alumina film and in alumina supported catalysts. *Appl. Surf. Sci.* **2005**, *252*, 1076−1083.
(71) Aronniemi, M.; Sainio, J.; Lahtinen, J. Chemical state quantification of iron and chromium oxides using XPS: The effect of the background subtraction method. *Surf. Sci.* **2005**, *578*, 108−123.

https://doi.org/10.1021/acsanm.3c01087
ACS Appl. Nano Mater. 2023, 6, 10178−10190

(72) Ikemoto, I.; Ishii, K.; Kinoshita, S.; Kuroda, H.; Alario Franco, M. A.; Thomas, J. M. X-ray photoelectron spectroscopic studies of CrO_2 and some related chromium compounds. *J. Solid State Chem.* **1976**, *17*, 425−430.
(73) Salvi, A. M.; Castle, J. E.; Watts, J. F.; Desimoni, E. Peak fitting of the chromium 2p XPS spectrum. *Appl. Surf. Sci.* **1995**, *90*, 333−341.
(74) Bullen, H.; Garrett, S. Epitaxial growth of CrO_2 thin films on TiO_2 (110) surfaces. *Chem. Mater.* **2002**, *14*, 243−248.
(75) Groot, F. De. Multiplet effects in X-ray spectroscopy. *Coord. Chem. Rev.* **2005**, *249*, 31−63.
(76) Montoro, L.; Abbate, M.; Almeida, E.; Rosolen, J. Electronic structure of the transition metal ions in $LiCoO_2$, $LiNiO_2$ and $LiCo_{0.5}Ni_{0.5}O_2$. *Chem. Phys. Lett.* **1999**, *309*, 14−18.
(77) Ikeno, H.; Tanaka, I.; Koyama, Y.; Mizoguchi, T.; Ogasawara, K. First-principles multielectron calculations of Ni $L_{2,3}$ NEXAFS and ELNES for $LiNiO_2$ and related compounds. *Phys. Rev. B: Condens. Matter Mater. Phys.* **2005**, *72*, 075123.
(78) Ogasawara, K.; Iwata, T.; Koyama, Y.; Ishii, T.; Tanaka, I.; Adachi, H. Relativistic cluster calculation of ligand-field multiplet effects on cation $L_{2,3}$ x-ray-absorption edges of $SrTiO_3$, NiO, and CaF_2. *Phys. Rev. B: Condens. Matter Mater. Phys.* **2001**, *64*, 115413.
(79) Van Der Laan, G.; Zaanen, J.; Sawatzky, G. A.; Karnatak, R.; Esteva, J. M. Comparison of x-ray absorption with x-ray photoemission of nickel dihalides and NiO. *Phys. Rev. B: Condens. Matter Mater. Phys.* **1986**, *33*, 4253−4263.
(80) Wang, H.; Ge, P.; Riordan, C. G.; Brooker, S.; Woomer, C. G.; Collins, T.; Melendres, C.; Graudejus, O.; Bartlett, N.; Cramer, S. P. Integrated X-ray L Absorption Spectra. Counting Holes in Ni Complexes. *J. Phys. Chem. B* **1998**, *102*, 8343−8346.
(81) Hu, Z.; Golden, M. S.; Fink, J.; Kaindl, G.; Warda, S. A.; Reinen, D.; Mahadevan, P.; Sarma, D. D. Hole distribution between the Ni 3d and O 2p orbitals in $Nd_{2-x}Sr_xNiO_{4-\delta}$. *Phys. Rev. B: Condens. Matter Mater. Phys.* **2000**, *61*, 3739−3744.
(82) Cherkashinin, G.; Motzko, M.; Schulz, N.; Späth, T.; Jaegermann, W. Electron spectroscopy study of Li[Ni,Co,Mn]O_2/electrolyte interface: Electronic structure, interface composition, and device implications. *Chem. Mater.* **2015**, *27*, 2875−2887.
(83) Kumagai, Y.; Ikeno, H.; Oba, F.; Matsunaga, K.; Tanaka, I. Effects of crystal structure on Co- $L_{2,3}$ x-ray absorption near-edge structure and electron-energy-loss near-edge structure of trivalent cobalt oxides. *Phys. Rev. B: Condens. Matter Mater. Phys.* **2008**, *77*, 155124.
(84) Hsu, S.-H.; Hung, S.-F.; Wang, H.-Y.; Xiao, F.-X.; Zhang, L.; Yang, H.; Chen, H. M.; Lee, J.-M.; Liu, B. Tuning the Electronic Spin State of Catalysts by Strain Control for Highly Efficient Water Electrolysis. *Small Methods* **2018**, *2*, 1800001.
(85) Guillou, F.; Zhang, Q.; Hu, Z.; Kuo, C. Y.; Chin, Y. Y.; Lin, H. J.; Chen, C. T.; Tanaka, A.; Tjeng, L. H.; Hardy, V. Coupled valence and spin state transition in $(Pr_{0.7}Sm_{0.3})_{0.7}Ca_{0.3}CoO_3$. *Phys. Rev. B: Condens. Matter Mater. Phys.* **2013**, *87*, 115114.
(86) Morales, F.; De Groot, F. M. F.; Glatzel, P.; Kleimenov, E.; Bluhm, H.; Haevecker, M.; Knop-Gericke, A.; Weckhuysen, B. M. In situ X-ray absorption of Co/Mn/TiO_2 catalysts for Fischer-Tropsch synthesis. *J. Phys. Chem. B* **2004**, *108*, 16201−16207.
(87) Ensling, D.; Cherkashinin, G.; Schmid, S.; Bhuvaneswari, S.; Thissen, A.; Jaegermann, W. Nonrigid band behavior of the electronic structure of $LiCoO_2$ thin film during electrochemical Li deintercalation. *Chem. Mater.* **2014**, *26*, 3948−3956.
(88) Abbate, M.; De Groot, F. M. F.; Fuggle, J. C.; Fujimori, A.; Tokura, Y.; Fujishima, Y.; Strebel, O.; Domke, M.; Kaindl, G.; Van Elp, J.; Thole, B. T.; Sawatzky, G. A.; Sacchi, M.; Tsuda, N. Soft-x-ray-absorption studies of the location of extra charges induced by substitution in controlled-valence materials. *Phys. Rev. B: Condens. Matter Mater. Phys.* **1991**, *44*, 5419−5422.
(89) Seong, S.; Lee, E.; Kim, H. W.; Min, B. I.; Lee, S.; Dho, J.; Kim, Y.; Kim, J. Y.; Kang, J. S. Experimental evidence for mixed-valent Cr ions in half-metallic CrO_2: Temperature-dependent XMCD study. *J. Magn. Magn. Mater.* **2018**, *452*, 447−450.
(90) Theil, C.; van Elp, J.; Folkmann, F. Ligand field parameters obtained from and chemical shifts observed at the Cr $L_{2,3}$ edges. *Phys. Rev. B: Condens. Matter Mater. Phys.* **1999**, *59*, 7931−7936.
(91) Dedkov, Y. S.; Vinogradov, A. S.; Fonin, M.; König, C.; Vyalikh, D. V.; Preobrajenski, A. B.; Krasnikov, S. A.; Kleimenov, E. Y.; Nesterov, M. A.; Rüdiger, U.; Molodtsov, S. L.; Güntherodt, G. Correlations in the electronic structure of half-metallic ferromagnetic CrO_2 films: An x-ray absorption and resonant photoemission spectroscopy study. *Phys. Rev. B: Condens. Matter Mater. Phys.* **2005**, *72*, 060401.
(92) Gaudry, É.; Sainctavit, P.; Juillot, F.; Bondioli, F.; Ohresser, P.; Letard, I. From the green color of eskolaite to the red color of ruby: An X-ray absorption spectroscopy study. *Phys. Chem. Miner.* **2006**, *32*, 710−720.
(93) Chang, C. F.; Huang, D. J.; Tanaka, A.; Guo, G. Y.; Chung, S. C.; Kao, S. T.; Shyu, S. G.; Chen, C. T. Electronic structure of CrO_2 studied by magnetic circular dichroism in resonant photoemission. *Phys. Rev. B: Condens. Matter Mater. Phys.* **2005**, *71*, 052407.
(94) de Groot, F. M. F.; Grioni, M.; Fuggle, J. C.; Ghijsen, J.; Sawatzky, G. A.; Petersen, H. Oxygen 1*s*x-ray-absorption edges of transition-metal oxides. *Phys. Rev. B: Condens. Matter Mater. Phys.* **1989**, *40*, 5715−5723.
(95) Kuiper, P.; Kruizinga, G.; Ghijsen, J.; Sawatzky, G. A.; Verweij, H. Character of Holes in $Li_xNi_{1-x}O$ and Their Magnetic Behavior. *Phys. Rev. Lett.* **1989**, *62*, 221−224.
(96) Chen, D.; Zhong, J.; Wu, X.; Wu, Z.; Mironova-Ulmane, N.; Kuzmin, A.; Marcelli, A. Oxygen K-edge XANES investigation of $Ni_cMg_{1-c}O$ solid solutions. *Spectrochim. Acta, Part A* **2008**, *70*, 458−461.
(97) Yang, Q.; Wang, J.; Lou, X.; Chen, Z.; Hu, B. Self-assembled 3D $Ni_xCo_{3-x}O_4$ pseudocube superstructure as potential anode material for Li-Ion batteries. *J. Alloys Compd.* **2020**, *814*, 152319.
(98) Abbate, M.; Zampieri, G.; Prado, F.; Caneiro, A.; Gonzalez-Calbet, J. M.; Vallet-Regi, M. Electronic structure and metal-insulator transition in $LaNiO_{3-\delta}$. *Phys. Rev. B: Condens. Matter Mater. Phys.* **2002**, *65*, 155101.
(99) Alves, E.; Martins, H. P.; Domenech, S.; Abbate, M. Band structure and cluster model calculations of $LaNiO_3$ compared to photoemission, O 1s X-ray absorption, and optical absorption spectra. *Phys. Lett. A* **2019**, *383*, 2952−2956.
(100) Yoon, W. S.; Kim, K. B.; Kim, M. G.; Lee, M. K.; Shin, H. J.; Lee, J. M.; Lee, J. S.; Yo, C. H. Oxygen contribution on Li-ion intercalation-deintercalation in $LiCoO_2$ investigated by O K-edge and Co L-edge X-ray absorption spectroscopy. *J. Phys. Chem. B* **2002**, *106*, 2526−2532.
(101) Kurata, H.; Lefèvre, E.; Colliex, C.; Brydson, R. Electron-energy-loss near-edge structures in the oxygen K-edge spectra of transition-metal oxides. *Phys. Rev. B: Condens. Matter Mater. Phys.* **1993**, *47*, 13763−13768.
(102) Carboni, M.; Brutti, S.; Marrani, A. G. Surface Reactivity of a Carbonaceous Cathode in a Lithium Triflate/Ether Electrolyte-Based Li-O_2 Cell. *ACS Appl. Mater. Interfaces* **2015**, *7*, 21751−21762.
(103) Carboni, M.; Marrani, A. G.; Spezia, R.; Brutti, S. Degradation of LiTfO/TEGME and LiTfO/DME Electrolytes in Li-O_2 Batteries. *J. Electrochem. Soc.* **2018**, *165*, A118−A125.
(104) Younesi, R.; Hahlin, M.; Björefors, F.; Johansson, P.; Edström, K. Li−O_2 Battery Degradation by Lithium Peroxide (Li_2O_2): A Model Study. *Chem. Mater.* **2013**, *25*, 77−84.
(105) Ferrari, I.; Motta, A.; Zanoni, R.; Scaramuzzo, F. A.; Amato, F.; Dalchiele, E. A.; Marrani, A. G. Understanding the nature of graphene oxide functional groups by modulation of the electrochemical reduction: A combined experimental and theoretical approach. *Carbon* **2023**, *203*, 29−38.
(106) Younesi, R.; Urbonaite, S.; Edström, K.; Hahlin, M. The cathode surface composition of a cycled Li-O_2 battery: A Photoelectron spectroscopy study. *J. Phys. Chem. C* **2012**, *116*, 20673−20680.
(107) Mourad, E.; Petit, Y. K.; Spezia, R.; Samojlov, A.; Summa, F. F.; Prehal, C.; Leypold, C.; Mahne, N.; Slugovc, C.; Fontaine, O.;

https://doi.org/10.1021/acsanm.3c01087
ACS Appl. Nano Mater. 2023, 6, 10178−10190

et al. Singlet oxygen from cation driven superoxide disproportionation and consequences for aprotic metal-O_2 batteries. *Energy Environ. Sci.* **2019**, *12*, 2559−2568.
(108) Pierini, A.; Brutti, S.; Bodo, E. Superoxide Anion Disproportionation Induced by Li^+ and H^+: Pathways to $^1O_2$ Release in Li−O_2 Batteries. *ChemPhysChem* **2020**, *21*, 2060−2067.
(109) Imanishi, N.; Luntz, A. C.; Bruce, P. *The Lithium Air Battery: Fundamentals*; Springer: New York, 2014.
(110) Qiao, R.; Chuang, Y. D.; Yan, S.; Yang, W. Soft X-Ray Irradiation Effects of Li_2O_2, Li_2CO_3 and Li_2O Revealed by Absorption Spectroscopy. *PLoS One* **2012**, *7*, e49182−e49188.
(111) Kobayashi, H.; Emura, S.; Arachi, Y.; Tatsumi, K. Investigation of inorganic compounds on the surface of cathode materials using Li and O K-edge XANES. *J. Power Sources* **2007**, *174*, 774−778.

https://doi.org/10.1021/acsanm.3c01087
ACS Appl. Nano Mater. 2023, 6, 10178−10190